

First observations of an ICME compressing Mercury's dayside magnetosphere to the surface

Reka M. Winslow¹, Noé Lugaz¹, Charles J. Farrugia¹, Catherine L. Johnson^{2,3}, Brian J. Anderson⁴, Carol S. Paty⁵, Nathan A. Schwadron¹, Lydia Philpott², Manar Al Asad²

¹*Institute for the Study of Earth, Ocean, and Space, University of New Hampshire, Durham, NH, USA*

²*Department of Earth, Ocean and Atmospheric Sciences, The University of British Columbia, Vancouver, BC, Canada.*

³*Planetary Science Institute, Tucson, AZ, USA.*

⁴*The Johns Hopkins University Applied Physics Laboratory, Laurel, MD, USA.*

⁵*Department of Earth Sciences, University of Oregon, Eugene, OR, USA.*

Mercury is the only planet in the inner solar system, other than Earth, that possesses a dynamo-generated global, albeit weak, magnetic field. As a consequence of this weak field and the planet's proximity to the Sun, the magnetosphere of Mercury is highly dynamic, especially during times of interplanetary coronal mass ejections (ICMEs), which travel at high speeds compared to the solar wind and carry mass and magnetic field from the Sun¹. It has been long hypothesized^{2,3} that the magnetic flux on Mercury's dayside may be completely eroded or compressed below the surface during extreme conditions. Here we report the first observations of an ICME compressing Mercury's dayside magnetosphere below the surface, accompanied by a $\sim 40\%$ increase in the peak planetary field and a $\sim 300\%$ increase in the

magnetotail field. These phenomena have not been observed at any planet to date, and they provide evidence that Mercury sometimes behaves as an unmagnetized airless body. The ICME plasma interacts directly with Mercury’s surface, weathering the regolith and sputtering particles into the exosphere. The collapse of Mercury’s dayside magnetosphere has important implications for the habitability of close-in exoplanets around M dwarf stars, as such events may significantly contribute to planetary atmospheric loss in these systems.

Mercury’s weak internal field⁴, described by a dipole with a moment of 190 nT R_M^3 (where R_M is Mercury’s radius), offset 0.2 R_M northward from the geographic equator^{5–8}, does not present a large obstacle to the solar wind. During average solar wind conditions, the magnetopause subsolar stand-off distance, R_{SS} , is 1.45 R_M from the planet’s center, and the bow shock subsolar stand-off distance is 1.96 R_M ⁹. These distances are largely controlled by solar wind parameters and are most strongly affected during ICMEs when conditions are extreme. Observations from the MErcury Surface, Space ENvironment, GEOchemistry, and Ranging (MESSENGER) spacecraft indicate that the magnetopause was likely below the planet’s surface during $\sim 30\%$ of ICME-affected MESSENGER orbits¹⁰.

Here we examine an ICME event at Mercury that shows unambiguous signatures of magnetopause compression well below the planetary dayside surface. The ICME was launched from the Sun on 11/29/2013, reached Mercury at 14:25:35 UT on 11/30/2013, and was observed in situ by the Magnetometer¹¹ onboard MESSENGER (Figure 1a). The ICME, and specifically the magnetic cloud substructure (beginning at 16:13:12 UT), affected two consecutive orbits around Mercury.

Because the magnetospheric perturbation was strongest during the first orbit, we analyze this orbit (orbit 2577) in detail (Figure 1a). The magnetic field direction in the magnetic cloud was predominantly southward, however, it had a northward component for ~ 30 mins prior to MESSENGER crossing into Mercury's magnetosphere on this orbit. Using the modified Newtonian approximation described in Winslow et al.¹⁰, we estimated the ram pressure, P_{ram} , to be ~ 260 nPa from the inbound magnetopause crossing on orbit 2577. In comparison, the average P_{ram} at Mercury is 14 nPa, nearly twenty times lower. From the ICME launch time at the Sun¹² and the arrival time at Mercury, we calculated the Sun-to-Mercury transit speed to be ~ 800 km s⁻¹, which together with the P_{ram} estimate yields a plasma number density of ~ 240 cm⁻³, compared to ~ 100 cm⁻³ on average.

The most remarkable effect of this ICME on Mercury was the compression of the dayside magnetopause below the surface (Figure 1 and Extended Data Figure 1) resulting from this very high P_{ram} . During noon-midnight orbits, MESSENGER regularly spent ~ 20 minutes sampling Mercury's low-latitude dayside magnetosphere, usually entering the magnetosphere at latitudes close to the equator. Even though MESSENGER was in a noon-midnight orbit during this ICME, the location of the dayside magnetopause crossing into the magnetosphere occurred at a high latitude of 84° N, a longitude of 50° , and an altitude of only ~ 400 km (Figures 1b,c, 2, and Extended Data Figure 2). Prior to this crossing, MESSENGER was at altitudes less than 400 km at more southern latitudes and the magnetosphere was not encountered. Less than 1 minute after crossing the magnetopause, MESSENGER crossed into the nightside magnetosphere. Thus unlike typical noon-midnight orbits, MESSENGER spent less than 1 minute in the dayside after crossing the

magnetopause, which explains the lack of a cusp crossing. No dayside northward magnetic field direction was observed in the magnetosphere (Figure 1b,c and Extended Data Figure 1). The field lines that MESSENGER sampled immediately after entering the magnetosphere are southward and sunward pointing, consistent with field lines in the high northern hemisphere close to and threading the night-side (Figure 3).

The established shape and location of Mercury’s magnetopause determined empirically provide further confirmation of the compression well below the planetary surface. The Shue et al.¹³ magnetopause model has been shown to fit Mercury’s average magnetopause shape well, under both nominal and extreme solar wind conditions^{9,10}. For the inbound and outbound aberrated magnetopause crossings on this orbit, the best-fit model yields an R_{ss} of $0.69 R_M$, i.e. a value that is well below the surface (Figure 2). Thus, the evidence clearly implies the utter absence of a dayside magnetosphere in this case (Figure 3).

Past studies using magnetohydrodynamic simulations of the Mercury-solar wind interaction have predicted such magnetospheric compression to the surface². Even taking into account induction effects¹⁴ in their simulations, Jia et al.¹⁵ found that the magnetopause stand-off distance was reduced to $1.04 R_M$ for a P_{ram} of 132 nPa, which is sufficient for the magnetopause to reach some of the southern dayside surface¹⁶. Given the much higher P_{ram} of 260 nPa estimated for the ICME in our study, it is unsurprising that it collapsed Mercury’s dayside magnetosphere.

Another remarkable effect of the ICME on Mercury’s magnetosphere is the $\sim 40\%$ increase in the observed spacecraft closest-approach field strength compared to orbits prior to, and after

the ICME (Figure 1a). We investigated whether this increased field strength could be attributed to an induction effect resulting from magnetospheric compression. Annual induction signals have been observed in MESSENGER data¹⁶ and larger signals are expected during times of extreme compression¹⁴. Self-similar compression of the magnetosphere, resulting in a change in subsolar distance from $1.6R_M$ to R_{ss} at or below the surface could result in an increase in the internal dipole moment of up to $\sim 25\%$, similar to the observed increase in the field strength. However, an induction effect would increase the magnitude of all three components close to the planet, which is not observed. Extended Data Figure 1 shows that the increase in the field is almost entirely due to an increase in B_X , which persists throughout the orbit. In contrast, the B_Y component is almost identical on both orbit 2577 and the orbit prior to the ICME arrival, and B_Z decreases slightly close to the planet. In the tail, the field magnitude is enhanced by a factor of ~ 4 on orbit 2577 compared to 2576, suggesting that very different tail conditions, not induction, dominate the observed signal.

Despite the enhancement in the magnetotail field during this event, we find no evidence for flaring of the tail (see Methods). This, together with the calculated tail flux of 2.73 ± 0.86 MWb (see Methods), consistent with the average value of 2.6 ± 0.6 MWb observed at Mercury⁷, shows that the increase in the magnetotail field strength is not caused by flux-loading of the tail. The absence of flaring implies that Dungey cycle magnetospheric convection did not substantially enhance the tail field, which is supported by the fact that there are only a few flux transfer events (FTEs)^{17,18}. These FTEs are observed shortly after the inbound magnetopause at high latitudes, indicating some high-latitude reconnection. Low-latitude reconnection is unlikely because of the lack of dayside magnetosphere. However, observations by the Fast Imaging Plasma Spectrometer

(FIPS)¹⁹ onboard MESSENGER indicate that plasma is present in the southern tail lobe (Extended Data Figure 2), likely convected into the magnetosphere through the plasma mantle or via lobe convection driven by high-latitude reconnection.

The calculated magnetotail current sheet density of 1000 nA m^{-2} for orbit 2577 (see Methods and Extended Data Figure 5) is an order of magnitude higher than during average solar wind at Mercury²⁰. It has been statistically established at Earth²¹, and also recently at Mercury²⁰, that an increase in P_{ram} increases the tail lobe field and therefore the magnetic pressure in the tail. The increased magnetic pressure in the northern and southern tail lobes causes the current sheet to thin and compresses the total current into a smaller volume thereby increasing the current density. The strong magnetotail current is likely the main source of the increase in the intrinsic planetary field at closest-approach resulting from the strengthened B_X component.

Recent observations of the exospheric Na emission pattern at Mercury detected diffused equatorial Na at times of ICME passage, in contrast to the more commonly observed two-peak pattern at high latitudes in both hemispheres²². The major driver of Na surface release is particle precipitation, thus it is expected that during average conditions most of the Na emission is in the cusp regions where the magnetic field is weakest and particle precipitation is common^{8,23–25}. However, compression of Mercury’s dayside magnetosphere to the surface allows ICME plasma to directly impact the dayside at low latitudes, thereby sputtering Na into the exosphere. Our observation of such compression, and the previously predicted rate of occurrence for compression to the surface of 30% of ICME cases¹⁰, provides evidence for a mechanism of Na-generation at

equatorial latitudes. Due to the collapse of the dayside magnetosphere (and likely the exosphere) and the complete dominance of ICME particles on Mercury’s dayside, the Na^+ number densities estimated from FIPS observations show no dayside equatorial Na^+ on orbit 2577 (Extended Data Figure 2). However, the following two orbits (Extended Data Figures 3 and 4) show increased densities over the pre-ICME levels on most of the dayside, indicating sputtering by the high density ICME.

Finally, the disappearance of Mercury’s dayside magnetosphere may have important implications for exoplanetary systems. M dwarfs, the most common type of star²⁶, can have high occurrence rates of stellar flares²⁷ and are known to typically host exoplanets²⁸. It is unknown whether the flare-to-CME ratio of M dwarfs is similar to that of the Sun²⁷. However, because the habitable zone of M dwarfs is ~ 10 times closer to the star than in our solar system, exoplanets in these zones are susceptible to possibly very frequent magnetic eruptive events. ICMEs at close proximity to the host star are likely to carry higher P_{ram} than that observed in this study, due to the increased ICME speed and density close to the star. We thus suggest that a habitable exoplanet around an M dwarf might require an intrinsic planetary magnetic field substantially stronger than that of Mercury to not lose its atmosphere over geologic timescales. It has also been suggested that tidally locked planets²⁹ may have inherently weaker magnetic moments³⁰, so that for close-in exoplanets stellar-flare activity and associated ICME interactions may significantly hinder the emergence and development of life.

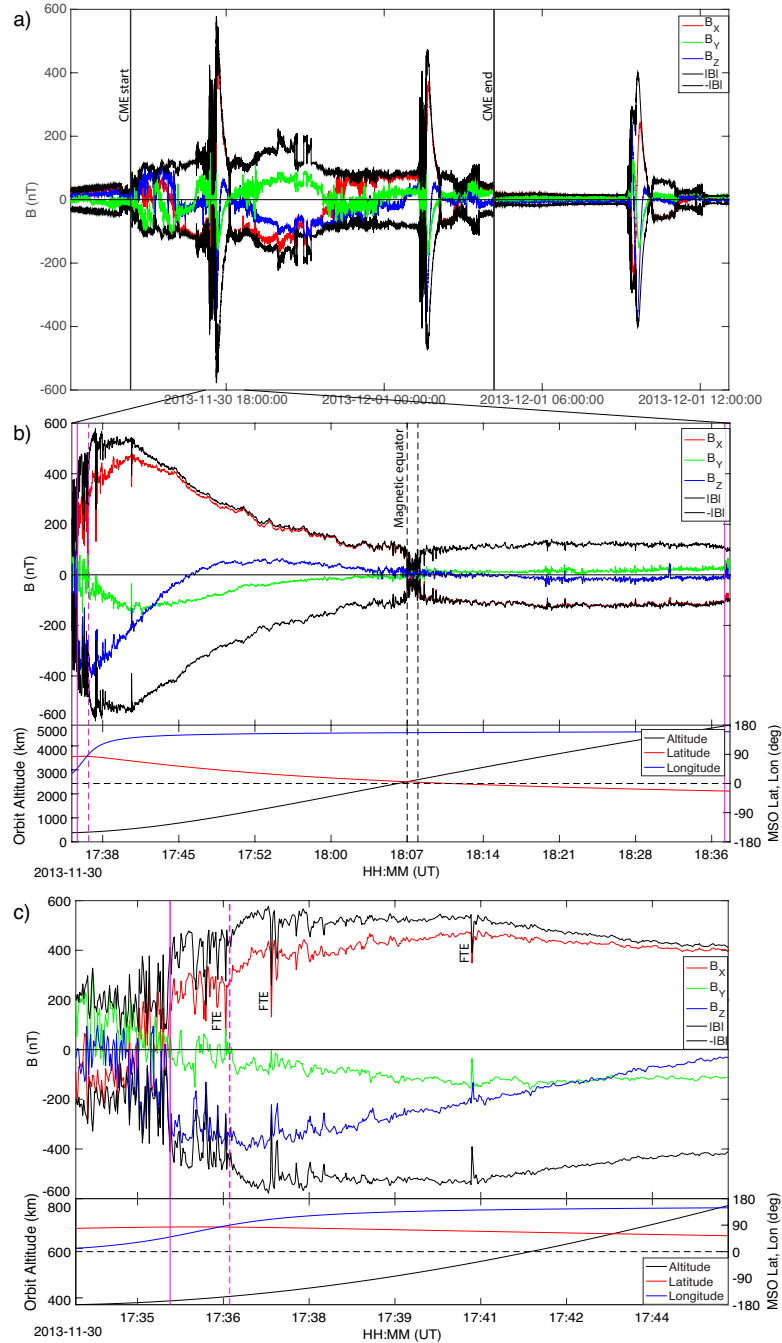


Figure 1: **MESSENGER magnetic field observations during the ICME impact at Mercury.**

a) Three orbits of MESSENGER around Mercury, with the ICME arrival and end marked by black vertical lines. b) The magnetospheric pass on the first orbit from panel a). Vertical solid magenta lines indicate inbound and outbound magnetopause crossings, while dashed magenta line indicates 90° longitude, i.e. beginning of the night-side transit. Vertical dashed black lines mark the magnetic equator crossing. c) The spacecraft closest approach region of the magnetospheric pass shown in b). Magenta lines are same as in b).

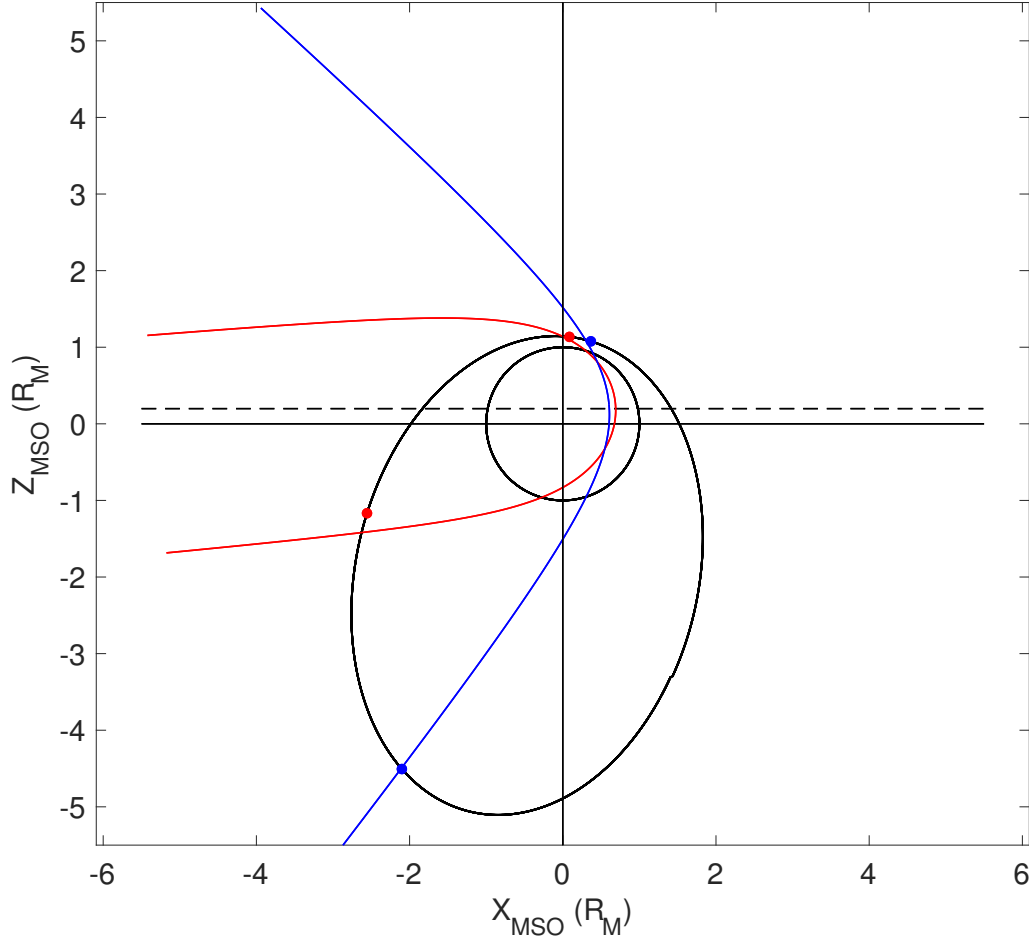


Figure 2: **MESSENGER's orbit and magnetospheric boundaries shortly after the ICME arrival.** MESSENGER's noon-midnight orbit around Mercury right after the ICME arrival is shown in black in the $Z_{MSO} - X_{MSO}$ plane. In MSO coordinates, X_{MSO} is positive sunward, Z_{MSO} is positive northward, Y_{MSO} is positive duskward and completes the right-handed system, and the origin is at the center of the planet. Best-fit magnetopause (red) and bow shock (blue) boundaries are shown, along with the tilt caused by the non-radial solar wind flow (see Methods). The magnetopause and bow shock boundary crossings are marked by red and blue dots, respectively. These crossings do not lie directly on the best-fit curves in the shown $Z_{MSO} - X_{MSO}$ plane because they were fit in the $\rho_{MSO} - X_{MSO}$ plane to take into account the small Y_{MSO} component. The dashed line represents the dipole offset of 484 km from the planetary equator.

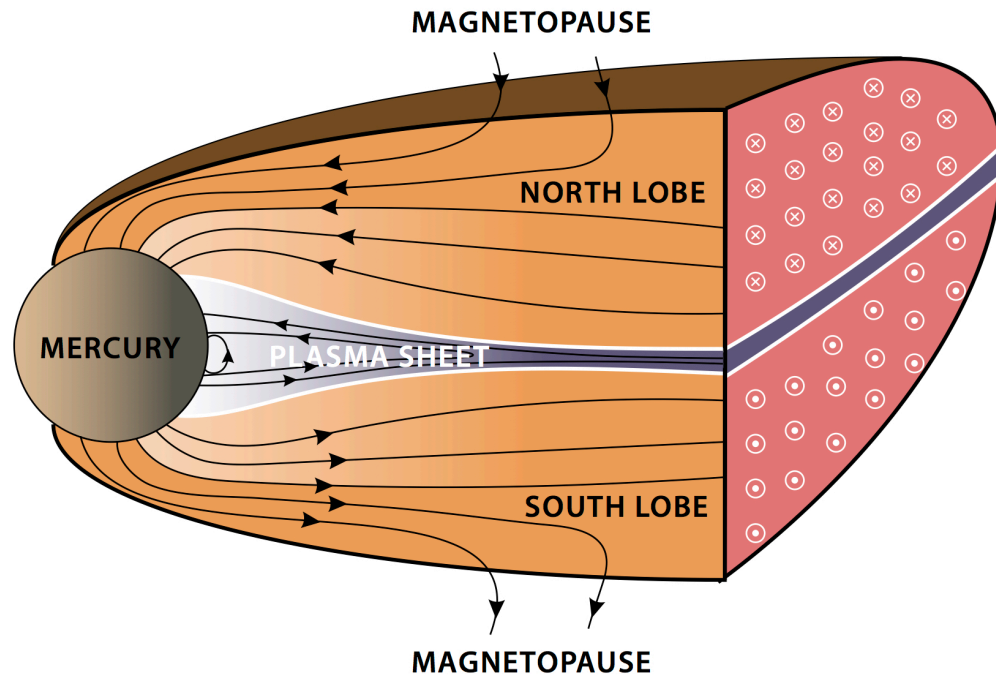


Figure 3: **Schematic view of Mercury's magnetosphere during the first ICME affected orbit.** The ICME compresses the dayside magnetosphere to the surface, leaving the region directly exposed to the solar wind.

Methods

MESSENGER's orbit, lack of dayside magnetosphere, and peak field. MESSENGER's highly eccentric orbit around Mercury (between March 2011 and April 2015) had periapsis altitudes between 200-500 km and apoapsis altitudes of 10,000-12,000 km. This allowed the spacecraft to spend a significant fraction of each orbit both in the solar wind and in the magnetosphere.

MESSENGER orbits 2576 (the orbit just prior to the ICME arrival) and 2577 (the first orbit affected by the ICME in question) were aligned in time on their equator crossing times (Extended Data Figure 1) to compare the magnetic field data before and after the ICME arrival. The increase in field strength in the nightside magnetosphere after the ICME arrival is evident from orbit 2576 to 2577, with peak field strengths of ~ 405 nT and ~ 575 nT on orbits 2576 and 2577, respectively. Furthermore, the almost complete absence of the dayside field on orbit 2577 compared to orbit 2576 is striking: the dayside northern hemisphere dipole field on orbit 2576 is seen via downward pointing (negative B_Z), anti-sunward (negative B_X) field, that is absent on orbit 2577.

Lack of tail flaring. Two lines of evidence support the inference of a magnetotail lacking substantial flaring during the passage of the ICME. First, the topology of the tail current sheet can be inferred from the direction of the field lines. A high amplitude of the B_Y and B_Z components relative to the B_X component imply that the tail is flared and can suggest tail loading. We calculated $|B_Y|/|B_X|$ ($|B_Z|/|B_X|$) in different regions of the tail (following Slavin et al.³), but no tail loading events were detected. We also calculated an average $|B_Y|/|B_X|$ (and $|B_Z|/|B_X|$) over the tail region for orbit 2577. For orbit 2576 (i.e., prior to the ICME arrival) the average $|B_Y|/|B_X|$

was 0.27 whereas on orbit 2577 the average $|B_Y|/|B_X|$ was 0.13 ($|B_Z|/|B_X|$ was even lower). This results from the dominant and large amplitude B_X on orbit 2577. The large static/thermal pressure in the sheath compressing the tail likely contributes to the observed lack of tail flaring at this time.

Second, the shape of the magnetopause boundary in the tail also provides information on the tail geometry. We fit the Shue et al.¹³ magnetopause model to the magnetopause boundary crossings inbound (high latitude northern hemisphere) and outbound (southern hemisphere) on this orbit to obtain the shape of the magnetopause, and therefore the magnetotail on this orbit (see next section for more details). The initial fit yielded a slightly flared ($\alpha = 0.58$; $\alpha = 0.5$ indicates no flaring) magnetopause due to the location of the outbound magnetopause crossing in the southern hemisphere. However, tilting of the tail southward due to non-radial ICME flows can cause the outbound magnetopause crossing to be observed farther south than it would be if there were no tail tilting, which can be mistaken for flaring of the magnetotail in an empirical fit.

We confirmed that the tail is actually tilted southward and not flared by comparing the location of the magnetic equator on this orbit with the average magnetic equator crossing location. Mercury's magnetic equator is observed on average³¹ at $Z = 484 \pm 3$ km, whereas on orbit 2577 the northernmost and southernmost crossings of the magnetic equator occurred at $Z = 463$ km and $Z = 347$ km respectively, both south of the average value.

The southward tilting of the magnetotail implies southward tilting of the field lines. To check that this is the case on this orbit, we calculated $\tan(B_Z/B_X)$ in the tail and found a $\sim 5^\circ$ downward

(i.e., southward) deflection of the field lines, in line with a southward tail tilting.

Further supporting the tilting of the tail is the fact that there were strong non-radial flows in the ICME. Although we do not have solar wind velocity and density data for this ICME at Mercury, the ICME was observed in longitudinal conjunction by STEREO A. The solar wind velocity at STEREO A shows strong excursions both north and south from radial flow (i.e. away from the ecliptic) during this ICME passage. We determined $\theta_{north-south}$, as described in Anderson et al.⁶ and found it to range between -9° and 12° at STEREO A, larger than the average non-radial solar wind flow at Mercury of 4° . As shown in Anderson et al.⁶, an average non-radial flow at Mercury is able to cause tail tilting. Given that we observe the magnetic equator southward of the average location, we can assume that at the time of the orbit in question MESSENGER is in the portion of the ICME that has a southward directed flow, with an average $\theta_{north-south}$ of $\sim -5^\circ$. We thus assume $\theta_{north-south} = -5^\circ$ during this time at Mercury, which is also supported by the observed degree of field line tilting in the tail as mentioned above. We correct the outbound magnetopause and bow shock crossing points for this extra aberration, by rotating the points clockwise by $\theta_{north-south}$. Fitting the Shue et al.¹³ model to the corrected magnetopause location yields a boundary with a non-flared magnetotail, i.e. a magnetopause with a flaring angle of $\alpha = 0.51$, consistent with the direct observations of extremely low $|B_Y|/|B_X|$ and $|B_Z|/|B_X|$ ratios at this time in the tail.

Empirical model fits to magnetopause and bow shock. Similarly to Winslow et al.^{9,10}, we fit empirical models to the magnetopause and bow shock crossing points to characterize the magnetospheric boundaries during orbit 2577. For the bow shock, we used a conic section given by

$$\sqrt{(X - X_0)^2 + \rho^2} = \frac{p\epsilon}{1 + \epsilon \cdot \cos \theta}, \quad (1)$$

where X_0 is the focus point, ϵ is the eccentricity, p is the focal parameter, and $\theta = \tan^{-1}(\frac{\rho}{X})$. For the magnetopause, we used the empirical model by Shue et al.¹³

$$R = \sqrt{X^2 + \rho^2} = R_{ss} \left(\frac{2}{1 + \cos \theta} \right)^\alpha, \quad (2)$$

where R is the distance from the dipole center and α is the flaring parameter that governs how open the magnetotail is.

We used these models to fit to our ICME-affected bow shock and magnetopause crossing locations, using a grid search method that minimized the root mean square (RMS) residual of the perpendicular distance of the observed boundary crossing from the model boundary. Although not the focus of the paper, these fits indicate that the bow shock was also substantially compressed on orbit 2577, having an estimated subsolar stand-off distance of $0.61 R_M$ with best-fit model parameters of $X_0 = 0$, $\epsilon = 1.46$, and $p = 1.02 R_M$.

For the model fits to the boundary locations, we used the instantaneous boundary crossings nearest to the magnetosphere for both the inbound and outbound crossings, and fit the inbound and outbound points with one model. It should be noted that fitting the inbound and outbound bow shock/magnetopause crossings with one bow shock/magnetopause model assumes that the solar wind conditions do not change substantially in the \sim hour between the inbound and outbound

observations. This assumption is not unreasonable for an ICME magnetic cloud passage, during which the solar wind plasma and magnetic field parameters are expected to vary more slowly than under average solar wind conditions.

Tail flux and tail current. We calculated the total magnetic flux in the tail from $\Phi_{Tail} = 0.5\pi B_{Tail} R_{Tail}^2$, where R_{Tail} , the cross-sectional radius of the tail, is 3905 ± 610 km and was calculated from the location of the midpoint of the outbound magnetopause crossing in the southern hemisphere (after correcting for the southward tilt of the tail). The error bar reflects the extent of the magnetopause layer. B_{Tail} was found to be 114.0 ± 5.2 nT and was calculated by averaging the magnitude of the magnetic field over 2 minutes prior to the outbound magnetopause crossing, with the uncertainty being the standard deviation of the field over the averaging period. This yields a total magnetic flux in the tail of 2.73 ± 0.86 MWb, consistent with the average value of 2.6 ± 0.6 MWb observed at Mercury⁷.

Tail current sheet (TCS) crossings were identified via a clear rotation in the field direction, specifically a rotation in B_X from sunward in the northern lobe to antisunward in the southern lobe, accompanied by a decrease in the total field strength $|B|$ and an increase in the high-frequency variability in the field³². The magnetic field data from orbit 2576 (Extended Data Figure 5, top left panel) show no evidence for a TCS crossing: B_X changes smoothly along the orbit as expected for a mainly dipolar internal field, and there is no decrease in $|B|$ near the equator crossing. Assuming that any TCS current flows mainly in the Y -direction, the current density, J_Y is proportional to $\Delta B_X / \Delta Z$. We computed $\Delta B_X / \Delta Z$ numerically along the orbit, and smoothed the estimate with a 30 second running mean. The resulting J_Y for orbit 2576 confirms no TCS crossing, i.e., on this

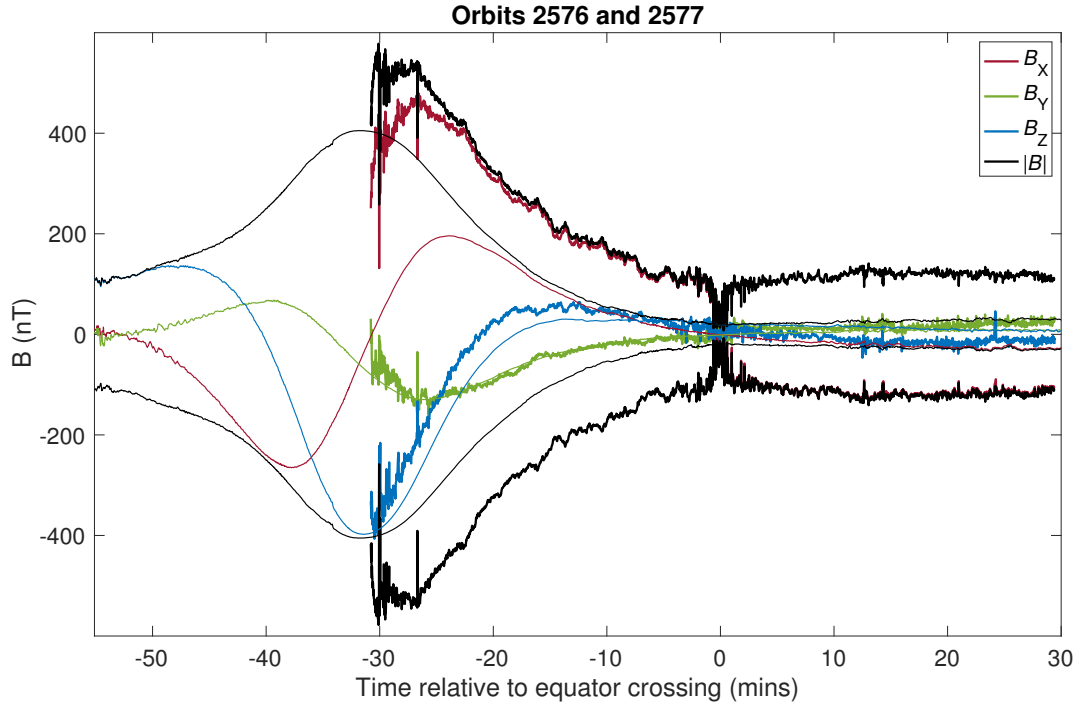


Figure 4: **Extended Data Figure 1: Comparison of MESSENGER's magnetospheric pass on the pre-ICME orbit with the first ICME affected orbit.** Magnetic field data versus time relative to the magnetic equator crossing times for orbits 2576 (thin lines) and 2577 (thick lines). Equator crossing times were at UTC 10:07:02 and UTC 18:07:49 for orbits 2576 and 2577, respectively.

orbit the magnetic equator crossing was planetward of the TCS. In contrast Orbit 2577 (Extended Data Figure 5, right) has a very different signature. The field magnitude in the tail lobe is ~ 125 nT, ~ 4 times that for the previous orbit. A pronounced dip in $|B|$ accompanies a reversal in B_X near the magnetic equator crossing. The inferred current density, J_Y shows a clear peak near $Z = 0$ km, reaching a maximum value over 1000 nA m^{-2} . This confirms that the tail current moved closer to the planet relative to the previous orbit and that the current density is particularly intense.

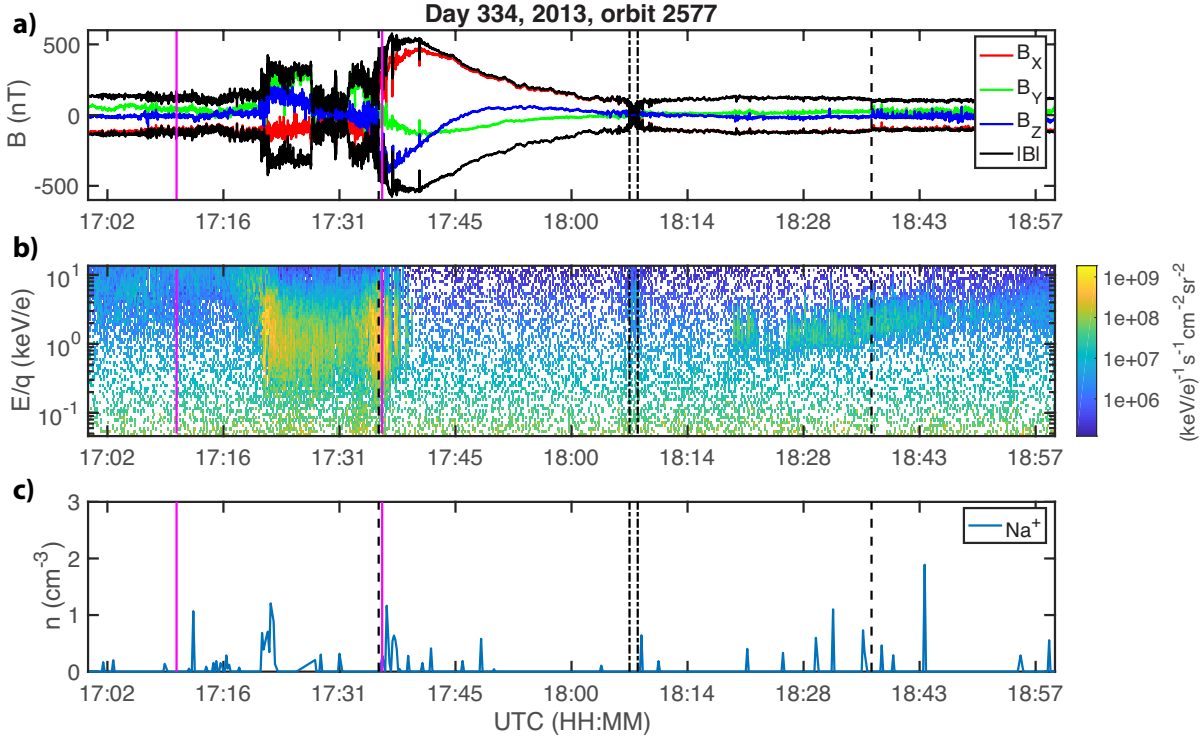


Figure 5: **Extended Data Figure 2: Proton and Na^+ observations by FIPS during orbit 2577.**

(a) Magnetic field data versus time for orbit 2577. The first magenta line marks the planetary equator, the second magenta line is near the North pole ($\sim 84^\circ$), the dashed black lines mark the magnetopause boundary, and the dot dashed lines mark the beginning and end of the magnetic equator. (b) Proton differential energy flux versus energy per charge (E/q) as a function of time. In the magnetotail, plasma is observed both near the magnetic equator crossing (consistent with the plasma sheet) and in the southern tail lobe prior to the outbound magnetopause crossing. (c) Na^+ density versus time. There are no density increases observed near equatorial latitudes on the dayside.

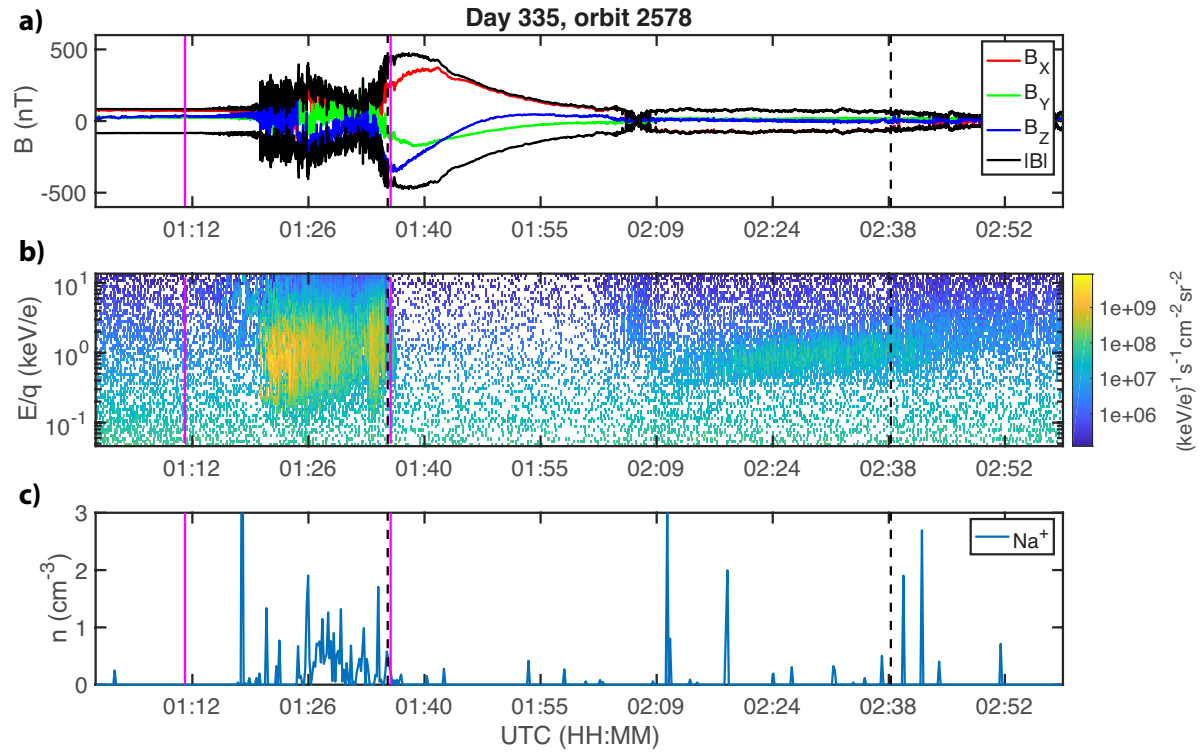


Figure 6: **Extended Data Figure 3: Proton and Na^+ observations by FIPS during orbit 2578.**

Same as Extended Data Figure 2 but for orbit 2578. Large density increases are observed near equatorial latitudes on the dayside.

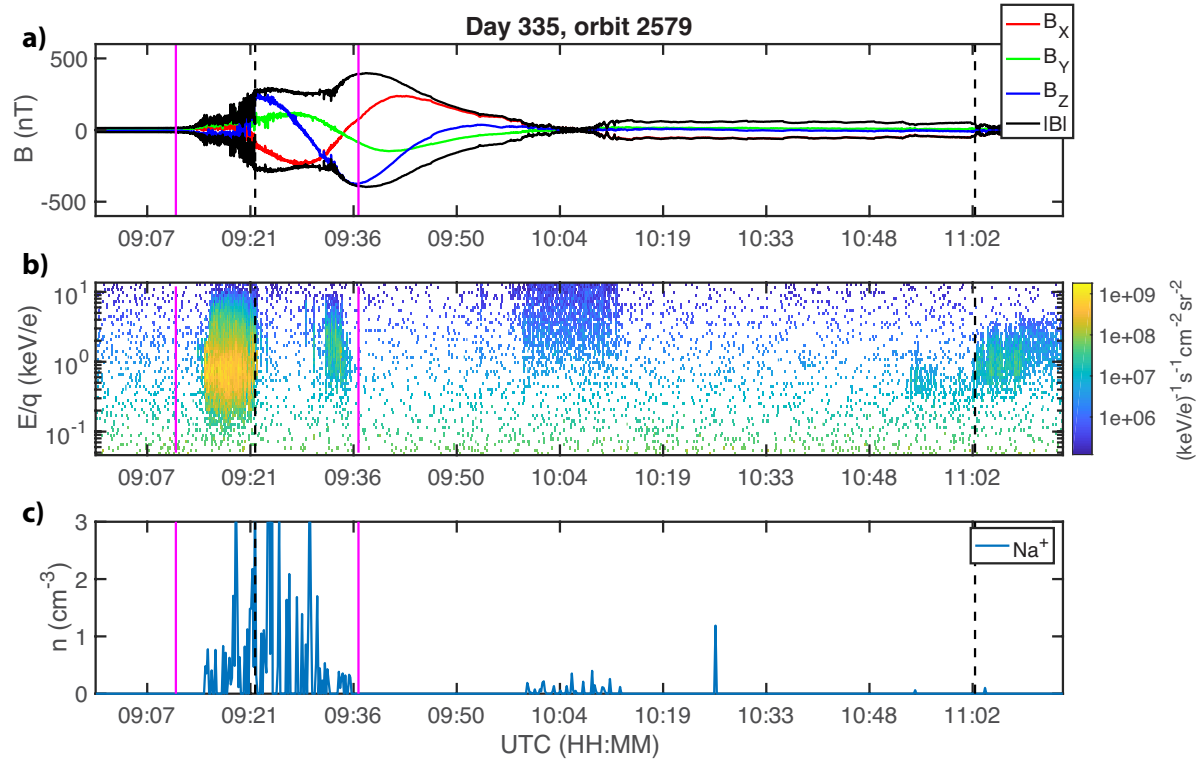


Figure 7: **Extended Data Figure 4: Proton and Na^+ observations by FIPS during orbit 2579.**

Same as Extended Data Figure 2 but for orbit 2579. Large density increases are observed near equatorial latitudes on the dayside.

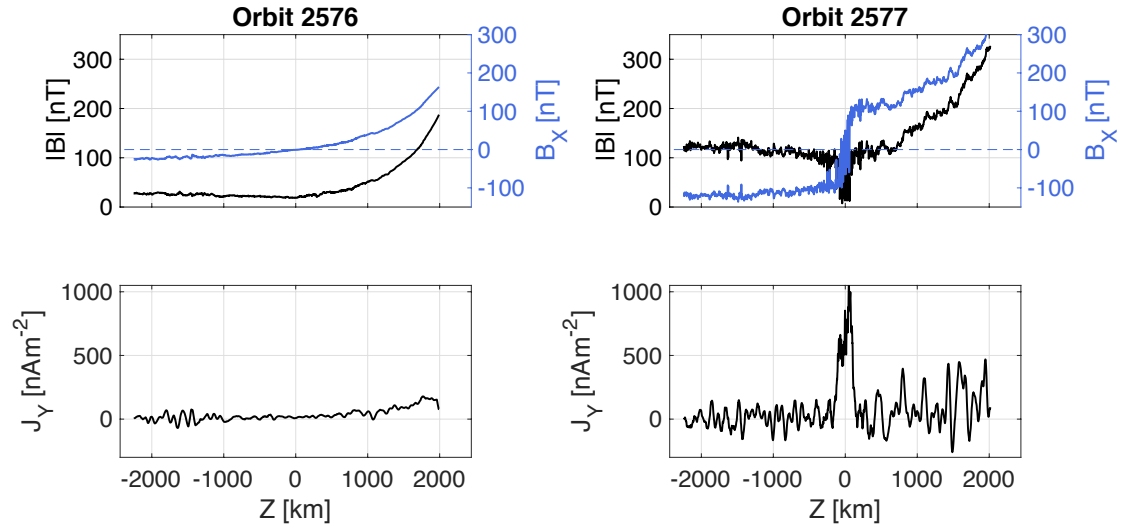


Figure 8: **Extended Data Figure 5: Magnetic field data and inferred current densities for orbits 2576 (left column) and 2577 (right column) versus distance in the Z direction.** The figures are centered on the magnetic equator crossing ($Z = 0$ km). Top row: B_X (blue) and $|B|$ (black) in nT. Bottom row: $J_Y = \Delta B_X / \Delta Z$.

1. Manchester, W. *et al.* The Physical Processes of CME/ICME Evolution. *Space Science Reviews* **212**, 1159–1219 (2017).
2. Kabin, K., Gombosi, T. I., DeZeeuw, D. L. & Powell, K. G. Interaction of Mercury with the Solar Wind. *Icarus* **143**, 397–406 (2000).
3. Slavin, J. A. *et al.* MESSENGER Observations of Extreme Loading and Unloading of Mercury’s Magnetic Tail. *Science* **329**, 665 (2010).
4. Ness, N. F., Behannon, K. W., Lepping, R. P. & Whang, Y. C. The magnetic field of Mercury. I. *Journal of Geophysical Research* **80**, 2708–2716 (1975).
5. Anderson, B. J. *et al.* The Global Magnetic Field of Mercury from MESSENGER Orbital Observations. *Science* **333**, 1859 (2011).
6. Anderson, B. J. *et al.* Low-degree structure in Mercury’s planetary magnetic field. *Journal of Geophysical Research (Planets)* **117**, E00L12 (2012).
7. Johnson, C. L. *et al.* MESSENGER observations of Mercury’s magnetic field structure. *Journal of Geophysical Research (Planets)* **117**, E00L14 (2012).
8. Winslow, R. M. *et al.* Mercury’s surface magnetic field determined from proton-reflection magnetometry. *Geophysical Research Letters* **41**, 4463–4470 (2014).
9. Winslow, R. M. *et al.* Mercury’s magnetopause and bow shock from MESSENGER Magnetometer observations. *Journal of Geophysical Research (Space Physics)* **118**, 2213–2227 (2013).

10. Winslow, R. M. *et al.* Statistical study of ICME effects on Mercury's magnetospheric boundaries and northern cusp region from MESSENGER. *Journal of Geophysical Research (Space Physics)* **122**, 4960–4975 (2017).
11. Anderson, B. J. *et al.* The Magnetometer Instrument on MESSENGER. *Space Science Reviews* **131**, 417–450 (2007).
12. Winslow, R. M. *et al.* Interplanetary coronal mass ejections from MESSENGER orbital observations at Mercury. *Journal of Geophysical Research (Space Physics)* **120**, 6101–6118 (2015).
13. Shue, J.-H. *et al.* A new functional form to study the solar wind control of the magnetopause size and shape. *Journal of Geophysical Research* **102**, 9497–9512 (1997).
14. Glassmeier, K.-H. *et al.* Electromagnetic Induction Effects and Dynamo Action in the Hermean System. *Space Science Reviews* **132**, 511–527 (2007).
15. Jia, X. *et al.* Global MHD simulations of Mercury's magnetosphere with coupled planetary interior: Induction effect of the planetary conducting core on the global interaction. *Journal of Geophysical Research (Space Physics)* **120**, 4763–4775 (2015).
16. Johnson, C. L. *et al.* MESSENGER observations of induced magnetic fields in Mercury's core. *Geophysical Research Letters* **43**, 2436–2444 (2016).
17. Russell, C. T. & Elphic, R. C. Initial ISEE magnetometer results - Magnetopause observations. *Space Science Reviews* **22**, 681–715 (1978).

18. Slavin, J. A. *et al.* MESSENGER observations of a flux-transfer-event shower at Mercury. *Journal of Geophysical Research (Space Physics)* **117**, A00M06 (2012).
19. Andrews, G. B. *et al.* The Energetic Particle and Plasma Spectrometer Instrument on the MESSENGER Spacecraft. *Space Science Reviews* **131**, 523–556 (2007).
20. Al Asad, M. M., Johnson, C. J. & Philpott, L. C. The Topology and Dynamics of Mercury's Tail Plasma and Current Sheets. In *Mercury: Current and Future Science of the Innermost Planet*, vol. 2047 of *LPI Contributions*, 6047 (2018).
21. Fairfield, D. H. & Jones, J. Variability of the tail lobe field strength. *Journal of Geophysical Research* **101**, 7785–7792 (1996).
22. Orsini, S. *et al.* Mercury sodium exospheric emission as a proxy for solar perturbations transit. *Nature Scientific Reports* **8**, 928 (2018). URL <https://doi.org/10.1038/s41598-018-19163-x>.
23. Winslow, R. M. *et al.* Observations of Mercury's northern cusp region with MESSENGER's Magnetometer. *Geophysical Research Letters* **39**, L08112 (2012).
24. Raines, J. M. *et al.* Structure and dynamics of Mercury's magnetospheric cusp: MESSENGER measurements of protons and planetary ions. *Journal of Geophysical Research (Space Physics)* **119**, 6587–6602 (2014).
25. Poh, G. *et al.* MESSENGER observations of cusp plasma filaments at Mercury. *Journal of Geophysical Research (Space Physics)* **121**, 8260–8285 (2016).

26. Henry, T. J. *et al.* The Solar Neighborhood. XVII. Parallax Results from the CTIOPI 0.9 m Program: 20 New Members of the RECONS 10 Parsec Sample. *The Astronomical Journal* **132**, 2360–2371 (2006). astro-ph/0608230.
27. Odert, P., Leitzinger, M., Hanslmeier, A. & Lammer, H. Stellar coronal mass ejections - I. Estimating occurrence frequencies and mass-loss rates. *Monthly Notices of the Royal Astronomical Society* **472**, 876–890 (2017). 1707.02165.
28. Dressing, C. D. & Charbonneau, D. The Occurrence Rate of Small Planets around Small Stars. *The Astrophysical Journal* **767**, 95 (2013). 1302.1647.
29. Kite, E. S., Gaidos, E. & Manga, M. Climate Instability on Tidally Locked Exoplanets. *The Astrophysical Journal* **743**, 41 (2011). 1109.2668.
30. Khodachenko, M. L. *et al.* Coronal Mass Ejection (CME) Activity of Low Mass M Stars as An Important Factor for The Habitability of Terrestrial Exoplanets. I. CME Impact on Expected Magnetospheres of Earth-Like Exoplanets in Close-In Habitable Zones. *Astrobiology* **7**, 167–184 (2007).
31. Johnson, C. L., Anderson, B. J., Korth, H., Phillips, R. J. & Philpott, L. C. Mercury’s internal magnetic field. In Solomon, S., Nittler, L. & Anderson, B. (eds.) *Mercury: The View after MESSENGER*, Cambridge Planetary Science (Cambridge University Press, 2018).
32. Slavin, J. A. *et al.* An ISEE 3 study of average and substorm conditions in the distant magnetotail. *Journal of Geophysical Research* **90**, 10 (1985).

Acknowledgements Support for this work was provided by NASA grant NNX15AW31G. R. M. W. acknowledges support from NASA grant NNX15AW31G and NSF grant AGS1622352. N. L. acknowledges support from NASA grants NNX15AB87G and NNX13AP52G. C. L. J., M. A. A. and L. P. acknowledge support from the Natural Sciences and Engineering Research Council of Canada.

Author Contributions R. M. W. developed the paper concept, performed the data analysis, interpretation and manuscript preparation. N. L., C. F., B. J. A., C. P. and N. A. S. contributed to data interpretation and general scientific evaluation. C. L. J. conducted the induction calculation. C. L. J. and M. A. A. calculated the magnetotail current and assisted with figure preparation. L. P. assisted with MESSENGER FIPS data analysis and figure preparation.

Competing Interests The authors declare that they have no competing interests.

Correspondence Correspondence and requests for materials should be addressed to R.M.W. (email: reka.winslow@unh.edu).